energies

MDPI

Article

A Dual-Function Design of an Oscillating Water Column Integrated with a Slotted Breakwater: A Wave Flume Study †

Clint C. M. Reyes [1], Mayah Walker [2], Zhenhua Huang [1,*] and Patrick Cross [3]

[1] Department of Ocean and Resources Engineering, University of Hawaii at Manoa, Honolulu, HI 96822, USA; ccreyes@hawaii.edu
[2] Department of Mechanical Engineering, University of Hawaii at Manoa, Honolulu, HI 96822, USA; mayahw@hawaii.edu
[3] Hawaii Natural Energy Institute, University of Hawaii at Manoa, Honolulu, HI 96822, USA; pscross@hawaii.edu
* Correspondence: zhenhua@hawaii.edu
† The material presented in this paper is based upon work supported by the Naval Facilities Engineering and Expeditionary Warfare Center (NAVFAC EXWC) under Contract No. N0002419D6400, Task Order No. N0002421F8805.

Abstract: Wave energy conversion holds promise for renewable energy, but challenges like high initial costs hinder commercialization. Integrating wave-energy converters (WECs) into shore-protection structures creates dual-function structures for both electricity generation and coastal protection. Oscillating water columns (OWCs) have been well studied in the past with their simple generation mechanism and their out-of-water power take-off (PTO) system, which can minimize bio-fouling effects and maintenance costs compared to other submerged WECs. In addition, a slotted barrier allows for better circulation behind the breakwater while dissipating incoming wave energy through viscous damping. This study examines the performance of a new design which combines an OWC with a slotted breakwater. Small-scale (1:49) laboratory tests were performed with a piston-type wave generator. The performance is evaluated in terms of wave transmission, wave energy extraction, and wave loading under various wave conditions while focusing on the effects of the porosity of the slotted barrier and tide level changes. Results show that under larger waves, a decreasing wave transmission, increasing power extraction from the OWC, and energy dissipation from the slotted barrier are observed. On the other hand, under increasing wavelengths, wave transmission is observed to be constant; this is important for harbor design, which means that the breakwater is effective under a wider range of wavelengths. Porosity allows for more transmission while inducing less horizontal force on the structure.

Keywords: wave energy conversion; shore protection; wave flume testing; oscillating water column; slotted barrier; breakwater

check for updates

Citation: Reyes, C.C.M.; Walker, M.; Huang, Z.; Cross, P. A Dual-Function Design of an Oscillating Water Column Integrated with a Slotted Breakwater: A Wave Flume Study. *Energies* **2024**, *17*, 3848. https://doi.org/10.3390/en17153848

Academic Editors: Vincenzo Franzitta, Daniele Milone, Domenico Curto and Andrea Guercio

Received: 31 May 2024
Revised: 18 July 2024
Accepted: 30 July 2024
Published: 5 August 2024

Copyright: © 2024 by the authors. Licensee MDPI, Basel, Switzerland. This article is an open access article distributed under the terms and conditions of the Creative Commons Attribution (CC BY) license (https://creativecommons.org/licenses/by/4.0/).

1. Introduction

The present study aims to address the following two issues in one solution: on one hand, our coastal infrastructure and property as well as precious beaches are put at risk by the projected sea-level rise and change in coastal wave conditions caused by climate change; on the other hand, our effort to combat climate change by reducing greenhouse emissions calls for a greater use of renewable energy, including wave energy. Breakwaters and seawalls are among the marine structures frequently used to protect shorelines. A dual function design of a breakwater integrated with wave-energy converters has the potential to address the two problems in one solution [1]. In addition, the availability of power from the breakwater can be used for local port operations or naval facilities.

There are many types of transitional breakwaters for shore protection and the construction of harbors [2]. Traditional gravity-type breakwaters such as rubble mounds may cause concerns

such as water stagnation [3]. Newer designs such as Bragg-type breakwaters [4–7], which reduce the harbor-side wave heights by inducing Bragg resonance, are effective only for a narrow frequency range. Additionally, such breakwaters require multiple structures in an array, leading to a high construction cost. Slotted breakwaters are relatively new concepts which allow the exchange of seawater between the sea side and the shore side of the breakwaters. The gaps in slotted barriers can be designed to allow fish to pass through and thus reduce potential adverse impacts of traditional breakwaters on local coastal ecosystems. The construction cost for this type of breakwaters can be lower than that for the traditional rubble mound breakwaters in relatively deep waters. A review on the wave interaction with slotted/perforated marine structures can be found in Huang et al. [8].

Ocean waves contain tremendous energy that has not been utilized [9]. Many technologies for using wave-energy converters (WECs) to generate electricity have been proposed [10,11]. Among existing WEC concepts, Oscillating-Water-Column (OWCs)-type WECs are one of the most studied and tested [10,12]. A Oscillating-Water-Column (OWC)-type WEC is chosen in this study for the integration with a slotted breakwater due mainly to prior extensive studies of pile breakwaters [1,13] and its simplistic working principle and design [14].

A typical OWC consists of a partially submerged, bottomless, pneumatic air chamber and out of water turbine [12]. Multi-chamber OWCs have also been proposed [15]. Typical slotted breakwaters/barriers consists of a thin plate with vertical or horizontal slots, which are usually affixed to the sea floor [16–18]. The dual function design to be examined in this study has an OWC supported by a bottom-sitting slotted barrier.

The use of numerical tools have been recently applied to further understand OWC structures, such as computational fluid dynamics (CFD) [19,20] and smoothed particle hydrodynamics (SPH) [21,22]. However, these numerical models are computationally expensive to run and still require validation using laboratory experiments prior to trusting the results. Thus, this study shall provide means of validation for such models, which is needed to optimize the design for the given site conditions. This work is also mainly focused on providing a new design of a slotted breakwater which integrates an OWC-type wave energy converter. This manuscript evaluates the performance of such a design in terms of wave transmission, wave energy extraction, and wave loading under various wave conditions, focusing on the effects of the porosity of the slotted barrier and tide level changes.

2. Methods

This section shall provide detail on the OWC–breakwater model and the experimental setup and tests, including the derivation of non-dimensional parameters to be used in the succeeding sections.

2.1. OWC–Breakwater Model

The OWC slotted barrier model affixed in the wave flume consists of a slotted barrier, an air chamber and an orifice in the top plate. A differential pressure sensor was mounted on the top, and a force balance was used to connect the model to a frame which was fixed to the flume, with the gaps being sealed to the flume walls with clay, as shown in Figure 1. The model is installed orthogonally to the bottom surface and the sidewalls of the flume. The structure was affixed at the rear to a single-axis force balance, which consists of 3 single-axis submbersible Futek load cells oriented in a triangular fashion in between two metal plates (see Figure 1). The force balance was precisely manufactured such that individual load cells are perpendicular to the plates so that no internal forces are generated by their orientation or installation. Special care was taken to make sure that the structure was not touching the wave flume. To seal the small gap between the flume bottom and the lower end of the slotted barrier, a thin flexible strip of foam was placed at the gap to avoid any unnecessary increase in the porosity of the slotted barrier. The foam material is very soft so that it will not affect the force readings.

The OWC air chamber and slotted barrier is 3D printed out of PLA. The Setra Model 239 differential pressure sensor has a high accuracy 0.073% FS and fast response time of <10 ms [23].

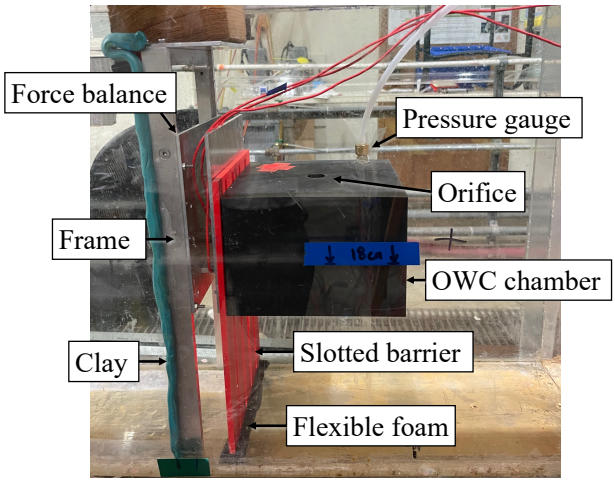


Figure 1. Model in a wave flume including an OWC air chamber, slotted barrier, pressure sensor, and force balance.

The dimensions of the OWC slotted barrier and air chamber are shown in Figure 2. The porosity of the slotted barrier is calculated for a fixed depth of 5.08 mm, height of 243.84 mm, width of 149.86 mm, and top and bottom borders of 5.08 mm, such that four equal slot widths varying for porosity are evenly distributed among the slotted barrier width. The OWC air chamber is 147.32 × 147.32 × 101.60 mm with a void volume of 1.80×10^6 mm^3. The orifice and pressure sensor circular openings at the top of the air chamber are 126.68 mm^2 and 143.14 mm^2, respectively. The orifice opening ratio is 0.88%. The opening for the pressure sensor is sealed with screw thread tape and clay.

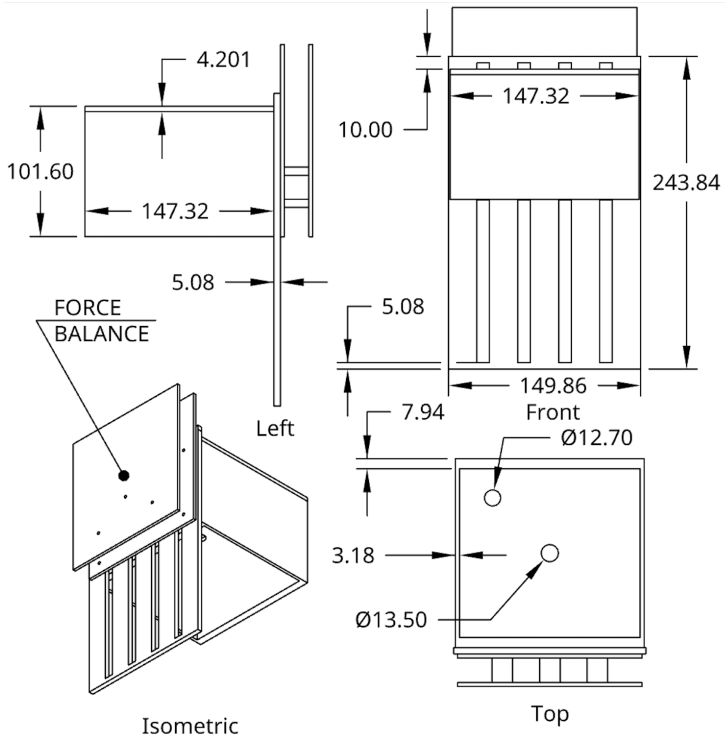


Figure 2. Dimensions [mm] of 25% porosity slotted barrier and OWC model with force balance.

2.2. Experimental Setup

Figure 3 shows the experimental setup used for this study. The wave flume used in this study is 8.0 m long, 0.5 m deep and 0.154 m wide. It is equipped with a piston-type wave-maker on one end and a wave-absorbing beach on the other end. The wave-absorbing beach is 2.1 m long and has a 1/10 slope. To further reduce the wave reflection, the slope was covered with an array of plastic cylinders, each with a diameter of about 1 mm. The OWC–breakwater model was installed in the middle section of the wave flume. Four capacitance-type wave gauges (G_1, G_2, G_3, G_4) are installed in the flume in two pairs on either side of the OWC slotted barrier model, as shown in Figure 3. The wave gauge pairs are spaced around 25 cm apart, while the distance between the wave gauge pairs and the structure (center to center) are about 2.15 m and 1.03 m for the seaward wave gauge pair and shoreward wave gauge pair, respectively.

These distances between the wave gauges were selected to avoid the influence of evanescent waves radiating from the structure. A pressure sensor was used to measure the air pressure inside the OWC air chamber, and a force balance built with three single-axis load cells was used to measure the wave force normal to the structure.

Note that the reason for using only two wave gauges for each location is limited by the data acquisition (DAQ) device used in the experiment having only eight differential channels. Wherein the pressure sensor uses one channel, and the force balance uses three channels, and this leaves four channels left for the wave gauges.

With regard to scaling, the structure dimensions are at an order of a 15 cm chamber width, while we can expect a full-scale breakwater with a width of about 7 m when testing at a 1:49 scale under Froude scaling. Note that this small scale makes it difficult to work with actual PTO systems, and thus, the use of an orifice as the PTO enables us to estimate the extracted power of the OWC at such a small scale. The underlying assumptions involved in using an orifice as a PTO are described in the succeeding subsection.

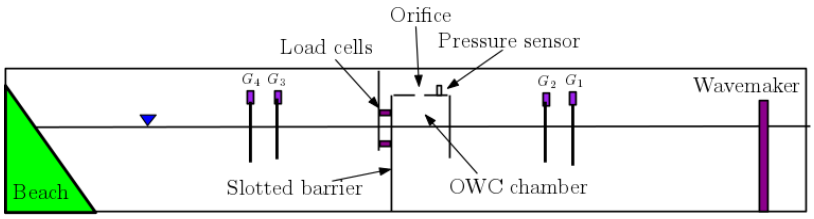


Figure 3. A sketch of the experimental setup. Not drawn to scale.

2.3. Calculations of Pneumatic Power and Extraction Efficiency

Since an orifice is used to model a nonlinear PTO in this small-scale experimental study, the difference of the air pressures inside and outside the air chamber, $p_a(t)$, can be parameterized by a quadratic loss coefficient C_f [24]

$$p_a(t) = \frac{1}{2}\rho_a C_f |u(t)|u(t), \tag{1}$$

where ρ_a is the density of the air, and $u(t)$ is the spatially averaged velocity of the air flow in the air chamber. For in-compressible air, this is equivalent to the spatially averaged velocity of the air–water interface inside the OWC chamber. Strictly speaking, the quadratic loss coefficient C_f needs to be determined experimentally. In this study, since the surface elevation inside the OWC chamber cannot be measured due to the small size of the model, the following empirical formula [24,25] is used with the assumption of a sharp-edged orifice,

$$C_f = \left(\frac{1}{\alpha C_c} - 1\right)^2, \tag{2}$$

where α is the opening ratio and C_c is the empirical coefficient of contraction given by

$$C_c = \frac{1}{0.639\sqrt{1-\alpha}+1}. \tag{3}$$

Using the experimental data available in the literature on OWC and orifice studies, Ulm et al. [26] argued that for the orifices used in the OWC studied, the dependence of C_c on the Reynold's number should be weak, and thus, C_c could be regarded as a function of the opening ratio α only.

The power of the incident waves in the wave flume, P_I, can be calculated by

$$P_I = EC_gW, \quad E = \frac{1}{2}\rho_w g A_I^2, \tag{4}$$

where E is the wave energy flux, C_g is the group velocity, W is the width of the wave flume, ρ_w is the water density, g is the gravitational acceleration, and A_I is the incident wave amplitude.

The pneumatic power generated by the OWC, P_{OWC}, is the work performed by the up-and-down motion of the air–water interface. Since the air pressure is nearly uniform inside the air chamber, P_{OWC} can be calculated by

$$P_{OWC} = A_{OWC}\overline{p_a(t)u(t)}, \tag{5}$$

where $A_{OWC} = WB$, with B being the distance between the front and back walls of the OWC chamber, while W is the cross-sectional area of the air chamber, and the overline represents a phase average (i.e., a time average over one wave period). He and Huang [25] have shown that the pneumatic power that can be extracted by the OWC, P_{OWC}, can be calculated by the measured air pressure inside the air chamber $p_a(t)$ alone using Equation (6),

$$P_{OWC} = A_{OWC}\sqrt{\frac{2}{\rho_a C_f}}\overline{|p_a(t)|^{3/2}}. \tag{6}$$

The performance of the (pneumatic) energy extraction by the model can be measured by the pneumatic efficiency ϵ, which is defined by

$$\epsilon = \frac{P_{OWC}}{P_I}, \tag{7}$$

which is in the range of 0 and 1. For brevity, it must be noted that the efficiency mentioned from hereon is the pneumatic efficiency and does not include mechanical losses due an actual PTO system.

2.4. Determination of Measured Reflection and Transmission Coefficients

The two-point wave separation method of Goda and Suzuki [27] is used to determine these three amplitudes in this study. A_I', A_R' and A_T' are the amplitudes of incident, reflected, and transmitted first harmonic waves. Wave reflection and transmission coefficients are two important design parameters for breakwaters. In this study, only regular waves are considered, and the reflection coefficient C_R' and the transmission coefficient C_T' are defined by

$$C_R' = \frac{A_R'}{A_I'}, \quad C_T' = \frac{A_T'}{A_I'}. \tag{8}$$

To improve the accuracy of the measured reflection and transmission coefficients, a correction was applied as shown below.

2.5. Wave Spatial Decay and Its Correction to Reflection and Transmission Coefficients

The reflection and transmission coefficients should be calculated using the amplitudes of the incident, reflected and transmitted waves measured at the OWC–breakwater. Due to the presence of evanescent waves and large eddies near the OWC–breakwater, the wave probes in the experiment cannot be placed close to the OWC–breakwater, which makes it difficult to obtain the wave amplitudes needed to accurately calculate the reflection and transmission coefficients. In practice, the wave probes are placed at a certain distance away from the OWC–breakwater; this distance is usually about several times the water depth. As a result, the reflection and transmission coefficients may carry systematic errors due to the spatial decay of the wave amplitude. This spatial attenuation can be caused by the wave boundary layers adjacent to solid boundaries [28], surface contamination [29,30], and the capillary hysteresis associated with the meniscus formed at the contact line [30].

Following Ippen [31] or Stiassnie et al. [32], the spatial decay of wave amplitude from $x = x_1$ to $x = x_2$ can be expressed as

$$A(x_2) = A(x_1)e^{-\beta\Delta x}, \quad \Delta x = |x_2 - x_1|, \tag{9}$$

where the spatial decay rate is denoted by β. Hunt [28] presented a theoretical expression for the spatial decay rate due to the solid boundaries of a rectangular channel. In this theory, the spatial decay rate β increases with decreasing channel width B and wave frequency ω as shown in Equation (10)

$$\beta = \frac{2k}{B}\sqrt{\frac{\nu}{2\omega}}\frac{kB + \sinh(2kh)}{2kh + \sinh(2kh)} \tag{10}$$

where k is the wave number, h is the water depth and ν is the kinematic viscosity of water. For a given wave period ω and flume width B, Equation (10) suggests a larger β value for a smaller h.

For the spatial decay rate due to surface contamination, Dorn [29] presented the following theoretical expression by assuming a horizontally immobilized surface,

$$\beta = \frac{2k}{B}\sqrt{\frac{\nu}{2\omega}}\frac{kB\sinh^2(kh)}{2kh + \sinh^2(kh)}. \tag{11}$$

The total spatial decay rate due to viscous damping should be the sum of the values given by Equations (10) and (11). However, these theoretical predictions do not agree with measurements well [29]. As a result, the spatial decay rate β is usually determined by performing empty wave-flume tests.

To correct the measured reflection and transmission coefficients with a given spatial decay rate β, we adopt the approach used by Stiassnie et al. [32]. We denote the amplitudes of the incident, reflected and transmitted waves at the OWC–breakwater as A_I, A_R and A_T. According to Equation (9), we have

$$A_I = A_I' e^{-\beta\Delta x_1}, \quad A_R' = A_R e^{-\beta\Delta x_1}, \quad A_T' = A_T e^{-\beta\Delta x_2}, \tag{12}$$

where Δx_1 is the distance between the OWC–breakwater structure and the wave gauges placed in front of the structure, and Δx_2 is the distance between the OWC–breakwater structure and the wave gauges placed after the structure. A constant spatial decay rate is assumed for incident, reflected and transmitted waves. Combining Equations (8) and (12) gives

$$C_R = C_R' e^{2\beta\Delta x_1}, \quad C_T = C_T' e^{\beta(\Delta x_1 + \Delta x_2)}. \tag{13}$$

Therefore, the actual reflection and transmission coefficients, C_R and C_T, are larger than those determined by Equation (8).

2.6. Determination of Viscous Loss Coefficient

The conservation of wave power says that the incident wave power is equal to the sum of the wave power in the reflected waves, the wave power in the transmitted waves, the pneumatic power extracted by the OWC and the wave power dissipated by viscous effects (i.e., vortex shedding). This can be expressed mathematically as

$$P_I = P_{OWC} + (C_T^2 + C_R^2)P_I + D_V, \tag{14}$$

where D_V represents the wave power dissipated by viscous effects. It then follows that the energy dissipation coefficient C_V can be calculated by

$$C_V = 1 - C_T^2 - C_R^2 - \epsilon, \quad C_V = D_V / P_I, \tag{15}$$

where both C_R and C_T are corrected using Equation (13) by a constant spatial decay rate for all test conditions.

2.7. Drag Coefficient

For engineering applications, we are mainly interested in the maximum wave force acting on the structure. Since weak nonlinearity is observed in the generated waves, wherein the crest is slightly larger than the trough, the analysis is focused on the maximum compressive force induced by the waves. Thus, the maximum compressive (positive) force measured under each wave was obtained and averaged over five wave periods. The force induced by the fluctuating water surface is then non-dimensionalized with the hydrodynamic pressure. Since we are only interested in the maximum force, we shall use the incident wave amplitude, which is assumed to be constant, to calculate the hydrodynamic pressure. This value is then assumed to be acting on the whole structure wherein the representative area is defined by the product of the still water depth and structure width. The non-dimensionalized force is given as

$$C_D = \frac{F_{x,max}}{Wh\rho_w g A_I}, \tag{16}$$

where $F_{x,max}$ is the average of the maximum values of the wave force $|F_x|$ in five stable waves, W is the width of the structure, and h is the still water depth.

2.8. Test Conditions and Procedure

Various wave conditions for small amplitude, long-crested, linear, and shallow water waves were tested to show the effects of porosity and tide levels on the extraction efficiency, wave energy, and wave loading for the OWC slotted barrier model. Four different slotted barrier porosities (10%, 15%, 20%, and 25%) were affixed at the same location to the OWC air chamber. Each slotted barrier model was tested at different water depths (16 cm, 17 cm, and 18 cm) representing tidal changes. For each water depth, 11 unique wave conditions were performed with one repeating test. The wave conditions, summarized in Tables 1–4, include a fixed wave amplitude at 1.0 cm with a varying period from 0.7 to 1.4 s with an interval of 0.1 s (Cases 1–8); and a fixed wave period 1.0 s with varying wave amplitudes of 0.5; 1.0; 1.5; and 2.0 cm (Cases 9–12). A fixed wave period of 1.0 s was used since it is the design wave period in this study. The wave conditions used can be mainly classified as 2nd-order Stokes waves except for wave Case 12, which is classified under 3rd-order Stokes, based on the classification of Zhao et al. [33].

The same test conditions were used for each porosity. Wave amplitudes were obtained by performing a wave separation analysis using the measured surface elevations. The data from the wave gauges, pressure sensor, and force balance were obtained by one DAQ at 100 Hz. Each test for a given wave condition yielded a 3 min time series, which consisted of about one minute of still water, one minute of waves, and one minute of still water.

Table 1. Measured amplitudes of incident waves [cm] for 10% porosity given three water depths (h) [cm] and period (T) [s] corresponding to the case number.

Case	**1**	**2**	**3**	**4**	**5**	**6**	**7**	**8**	**9**	**10**	**11**	**12**
$h \setminus T$	0.7	0.8	0.9	1.0	1.1	1.2	1.3	1.4	1.0	1.0	1.0	1.0
16	0.56	0.59	0.58	0.59	0.57	0.72	0.56	0.80	0.28	0.58	0.88	1.26
17	0.54	0.55	0.52	0.53	0.61	0.57	0.67	0.52	0.25	0.53	0.81	1.12
18	0.60	0.53	0.58	0.55	0.52	0.69	0.57	0.58	0.27	0.55	0.88	1.24

Table 2. Measured amplitudes of incident waves [cm] for 15% porosity given three water depths (h) [cm] and period (T) [s] corresponding to the case number.

Case	**1**	**2**	**3**	**4**	**5**	**6**	**7**	**8**	**9**	**10**	**11**	**12**
$h \setminus T$	0.7	0.8	0.9	1.0	1.1	1.2	1.3	1.4	1.0	1.0	1.0	1.0
16	-	-	-	-	-	-	-	-	-	-	-	-
17	0.54	0.53	0.54	0.53	0.60	0.58	0.59	0.54	0.27	0.55	0.84	1.16
18	0.58	0.56	0.61	0.60	0.53	0.81	0.56	0.59	0.27	0.57	0.90	1.26

Table 3. Measured amplitudes of incident waves [cm] for 20% porosity given three water depths (h) [cm] and period (T) [s] corresponding to the case number.

Case	**1**	**2**	**3**	**4**	**5**	**6**	**7**	**8**	**9**	**10**	**11**	**12**
$h \setminus T$	0.7	0.8	0.9	1.0	1.1	1.2	1.3	1.4	1.0	1.0	1.0	1.0
16	-	-	-	-	-	-	-	-	-	-	-	-
17	0.53	0.51	0.56	0.54	0.57	0.60	0.57	0.56	0.25	0.54	0.86	1.20
18	0.60	0.54	0.64	0.60	0.52	0.79	0.59	0.62	0.28	0.58	0.93	1.32

Table 4. Measured amplitudes of incident waves [cm] for 25% porosity given three water depths (h) [cm] and period (T) [s] corresponding to the case number.

Case	**1**	**2**	**3**	**4**	**5**	**6**	**7**	**8**	**9**	**10**	**11**	**12**
$h \setminus T$	0.7	0.8	0.9	1.0	1.1	1.2	1.3	1.4	1.0	1.0	1.0	1.0
16	0.53	0.57	0.61	0.64	0.59	0.65	0.62	0.71	0.29	0.61	0.97	1.36
17	0.51	0.54	0.56	0.57	0.56	0.72	0.56	0.58	0.27	0.54	0.87	1.21
18	0.57	0.52	0.64	0.61	0.54	0.71	0.53	0.63	0.30	0.62	0.96	1.34

2.9. Dimensional Analysis

To find out a set of dimensionless parameters to present the results, we present the following dimensionless analysis. The dimensionless parameters ϵ, C_R, C_T, C_V and C_D are functions of the following parameters

- Wave length (L), wave amplitude (A_I) and water depth h.
- The geometry of the OWC–breakwater. For geometrically similar models, the geometry of the OWC–breakwater model can be represented by the width of the OWC–breakwater B, which is the distance between the front and back walls of the OWC chamber.
- The porosity of the slotted barrier ϕ and the opening ratio of the orifice α.
- Density of the air ρ_a, density of water ρ_w, and gravitational acceleration g.

A dimensional analysis can lead to the following dimensionless relationships

$$(\epsilon, C_R, C_T, C_V, C_D) = f(L/B, A_I/B, h/B, \phi, \alpha, \rho_w/\rho_a) \tag{17}$$

In the experiment, both α and ρ_w/ρ_a are fixed. Therefore, the results for C_R, C_T, C_V, C_D and ϵ can be presented as functions of the following dimensionless parameters: dimensionless chamber width (B/L), dimensionless water depth (h/B), porosity of the slotted barrier (ϕ) and the dimensionless wave amplitude (A_I/B). Note that for a linear problem, the results should be independent of A_I/B.

3. Results

This section will cover the results of the wave decay parameter obtained from the empty flume tests, raw data collected from the wave gauges, pressure and force sensors, and the results obtained from the processed data in the form of the derived non-dimensional parameters from the previous section.

3.1. Spatial Decay Rates from Empty Wave Flume Tests

The spatial decay rate, β, is determined from empty flume tests, wherein two pairs of wave gauges are placed along the tank to obtain information on the waves passing at two different locations along the wave flume. Empty flume tests were performed for each wave condition at the low and high tide levels. Since the results only vary to an order of 0.01 under varying wave conditions, we shall assume a constant spatial decay rate, β, for each water depth condition. Here, the average β value of all the wave cases for each tide level shall be used. This value is 0.086 for 16 cm water depth and 0.060 for 18 cm water depth (Figure 4). The mean tide level case (17 cm) can be easily interpolated from the two results to be 0.073. These β values are then used in Equation (13) to correct the initially calculated reflection and transmission coefficients given in Equation (8).

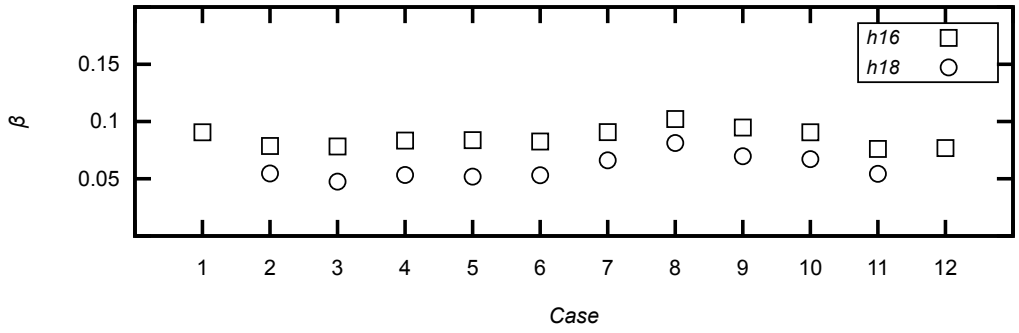


Figure 4. Energy dissipation parameter β for 16 and 18 cm water depths under varying wave cases.

3.2. Measured Surface Displacement, Pressure and Wave Loading

Figure 5 shows a snapshot of the raw data obtained from one of the experimental cases, wave Case 4 (Table 1), with a slotted barrier porosity of 10% and 18 cm water depth. The plotted data were collected synchronously throughout each test: water surface elevations η in two pairs: seaward (wave gauges 1 and 2), and shoreward (wave gauges 3 and 4) of the breakwater; air chamber pressure P, which is zeroed at the ambient air pressure; and total force F on the structure. The pressure and force data were smoothed using a low-pass frequency filter (MATLAB R2024a function: lowpass). A cut-off frequency of 2 Hz was used; note that the sampling frequency used was 100 Hz.

Experimental results are presented in terms of the dimensionless parameters derived in Section 2; these are plotted in Figures 6–9. Results are presented with a fixed slotted barrier porosity of 10% in Figures 6 and 7, since this represents an optimized porosity value [34] for the range of kh values in this experiment.

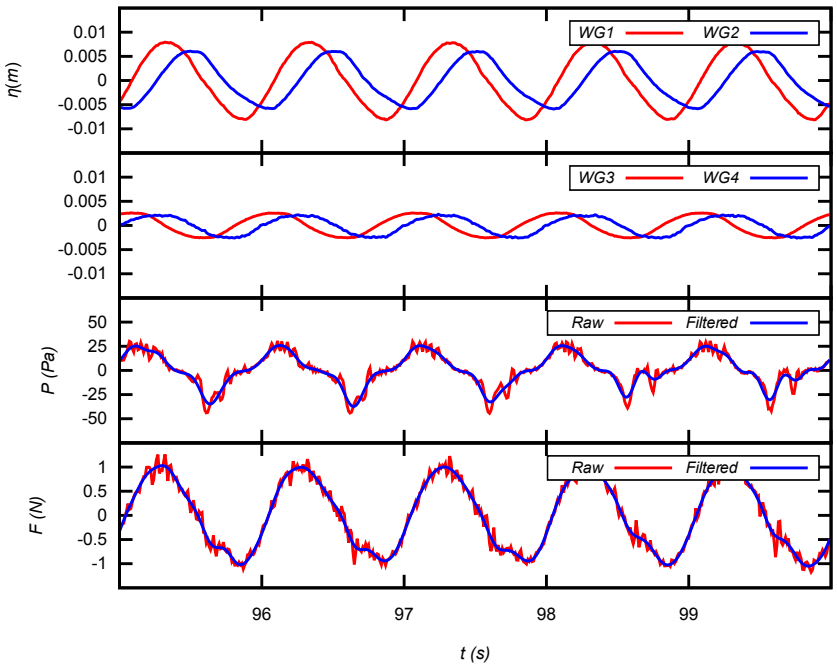


Figure 5. Sensor data obtained synchronously: water surface elevation (η), chamber pressure (P) and total force on structure (F) (wave Case 4, porosity is 10%, and 18 cm water depth).

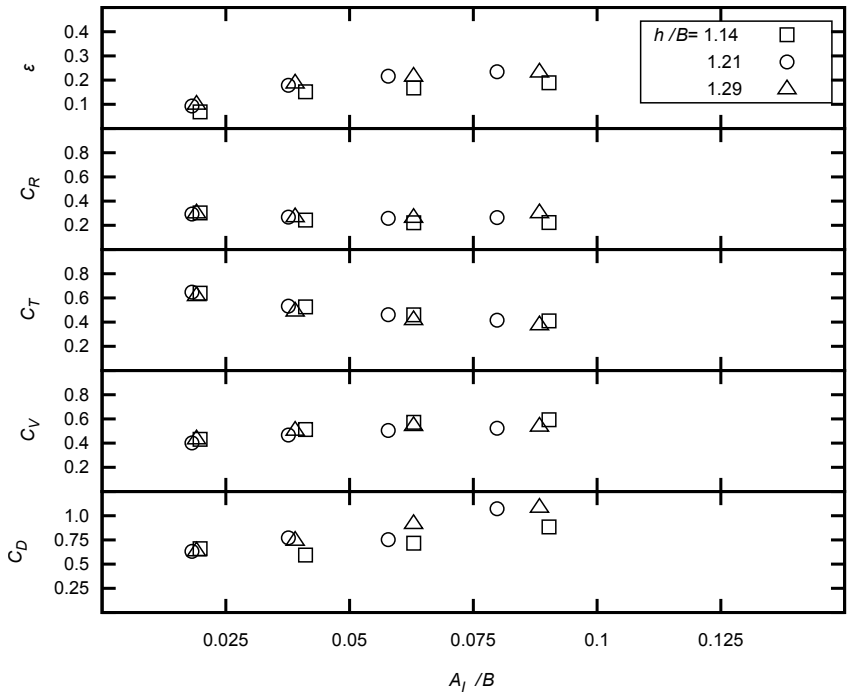


Figure 6. Various coefficients under varying wave heights and still water depths ($L/B = 8.17$, 10% porosity).

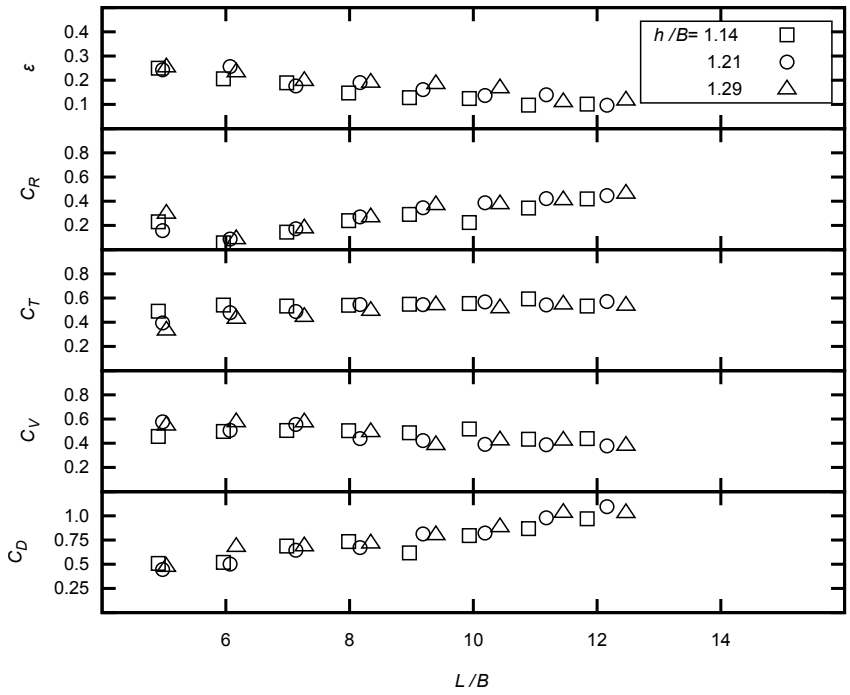


Figure 7. Various coefficients under varying wave periods and still water depths ($A_I/B = 0.038$, 10% porosity).

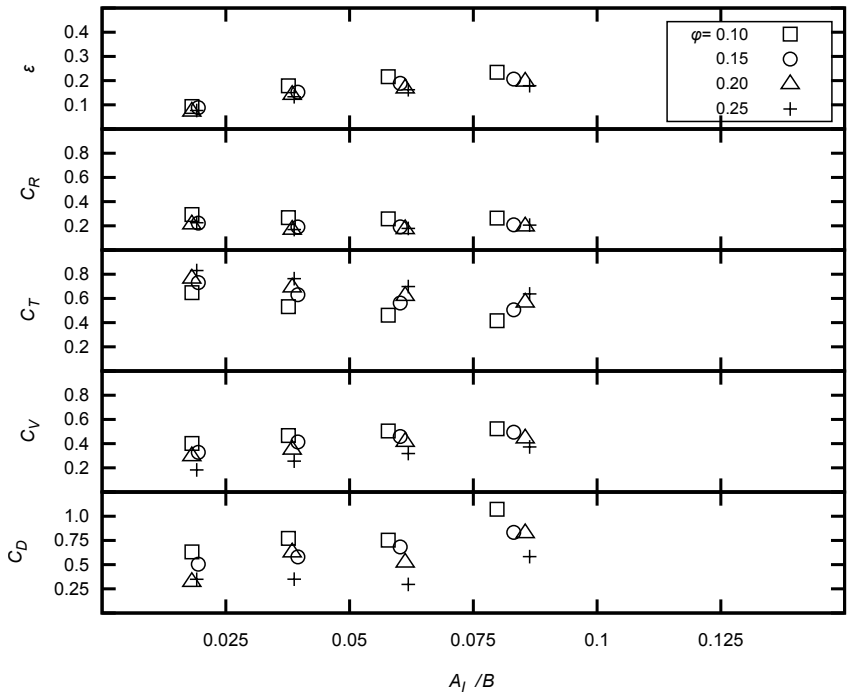


Figure 8. Various coefficients under varying incident wave height and porosity (L/B = 8.17, h/B = 1.21).

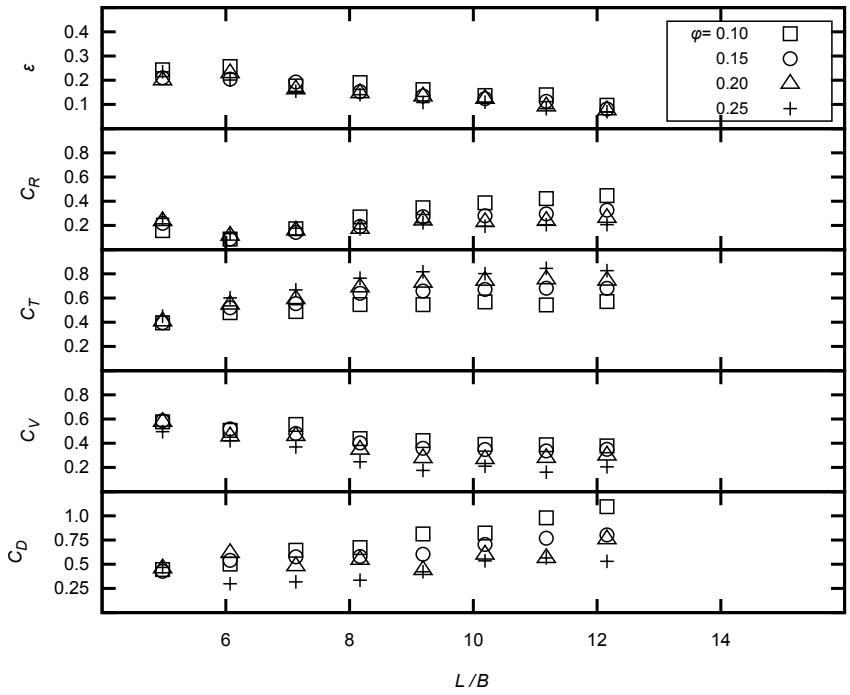


Figure 9. Various coefficients under varying wave periods and porosities ($A_I/B = 0.038, h/B = 1.21$).

3.3. Effects of Wave Amplitude

From Figure 6, we can observe that there is a nearly linear increase in the energy efficiency with the wave amplitude, given that incident waves are weakly nonlinear (2nd-order Stokes). This is further explained in the Discussion section, where we show that the energy efficiency is directly proportional to the wave amplitude. We also observe that with an increasing wave amplitude, there is a decrease in the transmission coefficient. In contrast, the reflection coefficient is observed to be constant under changing wave heights. Furthermore, the amount of energy dissipated by the slotted barrier is observed to be kept at a constant value under increasing wave amplitudes. Finally, the total horizontal force on the structure is naturally observed to increase as the wave amplitude increases.

3.4. Effects of Wave Period

Under varying wave periods (Figure 7), we observe the effect of multiple reflection at the front wall of the chamber. This is seen with the drop in the reflection coefficient to zero. For this case, it occurs at a wavelength to width ratio (L/B) of around 5. Minimal changes are observed for the transmission coefficient with a slight decrease under shorter wavelengths. The constant transmission coefficient is possible, since the increasing reflection (under longer waves) is balanced by the decrease in the energy efficiency of the OWC. The dissipation coefficient is also observed to be fairly constant for varying wave lengths. Finally, the maximum horizontal force on the slotted barrier is observed to increase under longer waves.

3.5. Effects of Water Depth

The effects of water depth changes are observed to be small for most cases (Figures 6 and 7). Slightly lower efficiency is observed for deeper water. A lower force coefficient is also observed for deeper water under a larger wave height. However, these changes tend to zero for lower wave heights. The transmission coefficient is closer to a constant value for deeper water under varying periods, while a slight decrease is observed for shorter waves in shallower water. This decrease, on the other hand, tends to zero as the wave length increases. Overall, these effects are shown to be of minimal importance for water-level changes at the scale of astronomic tides.

3.6. Effects of Slotted-Barrier Porosity

Now, we look into the effects of varying slotted barrier porosities on the non-dimensional parameters. Here, a porosity, ϕ, of 0.0 corresponds to an impermeable wall, and a porosity of 1.0 (100%) corresponds to full transmission. Figures 8 and 9 show that by decreasing the porosity, we observe an increase in the reflection coefficient. This also leads to an increase in viscous damping by the slotted barrier. In contrast, a decrease in the transmission coefficient is observed. For the energy extraction efficiency, no effect is observed for small-amplitude waves, while we see a very small increase in extraction efficiency for decreased porosities under larger amplitudes. Finally, we observe a larger horizontal force on the structure for decreasing porosity.

The effects are observed to be similar under varying wavelengths, wherein a more significant effect is observed for the reflection, transmission, dissipation, and force coefficients under long waves. Furthermore, the effects of slotted barrier porosity on the energy extraction efficiency is observed to be relatively smaller compared to the other coefficients. It must also be noted that for the extraction efficiency, the effect of the change in porosity under varying wavelengths is observed to be insignificant contrary to other parameters wherein the effects are more pronounced under longer waves. On the other hand, minimal effects are observed under shorter waves.

Lastly, repeating tests were performed for certain wave conditions and showed that the relative variation of the incident wave amplitude, reflection, and transmission coefficients is limited to the range of $\pm$5%.

4. Discussion

We have observed the effects of varying wave height, wave length, water depth, and slotted barrier porosity on each of the relevant non-dimensional parameters. In this section, we shall attempt to further elaborate and theorize the reasons behind the observed results in the previous section.

The nonlinear decrease of the reflection coefficient under varying wavelengths is observed, which occurs at around L/B = 6.0. This can be explained by the effect of multiple reflections between the front face of the OWC chamber and the slotted barrier. Waves reflect between both vertical walls at a distance apart, producing a partial standing wave inside the chamber, leading to a reduced reflection coefficient. Thus, it should occur theoretically when the width of the chamber is 1/4 of the wave length, which of course may be affected by the viscous effects. Our results show that the effect of multiple reflections may have occurred when the width of the chamber is about 1/6 of the wavelength. Similar studies have also been performed for an OWC with a rear vertical wall [35], wherein the reduction of the reflection coefficient occurs at around 1/5 of the wavelength.

The transmission coefficient, C_T, is observed to be fairly constant under the lowest porosity case (10%), which applies to the tested L/B values from 5 to 12. This range decreases during higher tide levels (Figure 7) and higher porosities (Figure 9). This constant property of the C_T value for a wide range of wavelengths is an interesting finding since this is unconventional for typical breakwaters. The constant wave transmission coefficient may be useful to harbor planners, since it shows that the design is effective for a wide range of wave periods. The possible cause of this phenomena for an OWC–breakwater shall be discussed in the succeeding subsection. Moreover, it must be noted that in the field, these results cannot be applied at the gaps or the heads of the breakwater. This is mainly due to wave diffraction and the fact that the results are limited to 1D flume experiments.

The constant reflection coefficient means that the reflected wave amplitude is linear with the incoming wave amplitude. This shows that the wave reflection is constant in amplitude for weakly nonlinear waves. On the other hand, all other parameters are variable under small changes of the wave amplitude. This shows the nonlinearity of the wave amplitude with respect to the other parameters. This is expected, since the wave energy is directly proportional to the square of the wave amplitude (or wave height). Also,

note that the scale of the wave amplitude with respect to B, A_I/B in contrast to L/B is much smaller, which is an order of 10^{-3}.

From varying the amplitude of the wave, we observe an increase in the energy efficiency of the OWC and the dissipation through the slotted barrier, which leads to a decrease in the wave transmission. This observation for the transmission coefficient is not typical for traditional breakwaters, and so this result is thought to be mainly due to the presence of the OWC and the slotted barrier. The efficiency is related to the power extracted, which is related to the square of the velocity, u^2. We also know that the energy dissipated by viscous damping through the slotted barrier is related to u^2 [36]. From this, we can see that an increase in the velocities, which is driven by the increase in the wave height, creates higher flow speeds at the chamber orifice and slots of the slotted barrier. This leads to an increased power extracted from the OWC (as well as extraction efficiency) and dissipation due to the slotted barrier.

We can see that the orifice at the top of the chamber, which acts as a power take-off (PTO), seems to have a similar effect as the slots of the slotted barrier, both of which have been modeled as a damper which applies viscous damping to the flow simply by introducing turbulence to the flow. This direct relationship of the velocity and wave amplitude with the energy extracted or dissipated by flow-damping orifices or slots is also the reason why for constant wave amplitudes and varying wave periods, the transmission coefficient is kept at a consistent value.

We note from Equation (5) that the power output, P_{OWC}, is directly related to the cube of the wave steepness,

$$P_{OWC} \propto \rho_a C_f A_{OWC} (\omega A_i)^3. \tag{18}$$

Since the incident wave power is proportional to A_i^2, the extraction efficiency as defined by Equation (7) can be formally written as

$$\epsilon = \kappa(L/B, C_f, h/B, \phi) A_i/B \tag{19}$$

The change of the pneumatic efficiency with wave amplitude shown in Figure 8 confirms Equation (19).

The results show that increasing h/B or decreasing ϕ can slightly increase the value of κ when all other dimensionless parameters are fixed. The results also show κ decreases almost linearly with increasing L/B when all other dimensionless parameters are fixed. If we write $\kappa \approx a(b - L/B)$ with $b > L/B$ and both a and b are positive functions of $h/B, \phi$ and C_f, we have

$$\epsilon \approx a(b - L/B) A_i/B. \tag{20}$$

We remark that A_i/B and L/B are not independent for ocean waves, and there might be a statistical relationship between wave height and period [37,38]; therefore, increasing L/B does not necessarily decrease the efficiency ϵ for ocean waves.

The effects of water-level change due to tides have been observed to be small and negligible for C_R, C_T, C_V and C_D. This is possibly due to the relative scale of the tidal range with respect to the water depths being small, which is of an order of 0.1. On the other hand, the effect of decreasing the porosity leading to a higher reflection coefficient and lower transmission coefficient is intuitive and can be seen as similar to that of the extreme case of an impermeable vertical wall with a porosity of 0.0, which can induce maximum reflection and minimum transmission—or the case with no wall at all (a porosity of 1.0), which allows for maximum transmission and minimum reflection.

The force coefficient C_D values obtained are around the range of 0.0 to 1.1. This is a good indication, since this coefficient can also serve as a safety factor that can easily be applied to engineering design. The range of values being close to 1.0 is a good indication, since this allows us to easily apply safety factors to the force coefficient, which is typically performed in engineering design. Do note that these results are limited to wave conditions, A_I/B from 0.05 to 0.2 and L/B from 9 to 18. Engineers might also be interested in the actual scale values of the extractable power by the OWC. Based on the experimental results,

the power extracted when scaled up to a 10 m wide chamber, with a 10% porous slotted wall, at 11 m water depth when subjected to 0.8 m high waves at 8 s is in the order of 7.5 kW. Note that this value is the power generated per unit length of chamber, and that power is based on pneumatic power, which does not involve mechanical losses. In addition, effects of air compressibility at full scale may slightly reduce the energy efficiency of the OWC. Related experiments have found that this reduction is around 5%.

The particles acted upon by waves move in a circular-like motion, and due to the presence of the OWC chamber, they will naturally absorb a significant vertical loading and transfer it to the structure foundation, which can also contribute to the moment induced at the base of the structure. Thus, future tests must include measurements of the vertical load on the structure.

Note that we are testing at a scale of 1:49 under Froude scaling, and that most of the assumptions involve neglecting the effect of varying Reynolds number. However, when scaling up, we must eventually consider a possible change in the effects of the Reynolds number. This may possibly impact our assumptions for a sharp-edged orifice. Thus, actual measurements of the velocity of the water surface inside the chamber would be necessary. Another means of measurement would be the use of an actual PTO system. The findings from this study are limited to the range of wave conditions presented in the Results section, which in the form of the dimensionless parameters presented are A_I/B values from 0.05 to 0.2 and L/B values from 9 to 18. For a 10 m wide chamber, this corresponds to incident wave amplitudes, A_I, from 0.05 to 0.2 m and wave periods, T, from 7 to 14 s.

5. Conclusions

A new dual-function energy absorbing (OWC-type) slotted breakwater was studied experimentally. Second (2nd)-order Stokes waves were predominantly used in the experiment except for wave Case 12 (3rd-order Stokes). The focus was on the effect of wave conditions and tide level changes on the pneumatic efficiency, wave transmission, wave loading, and wave energy dissipation due to a vortex generated by flow through a slotted barrier. The power takeoff was parameterized by an orifice of an opening ratio of 1%, and four slotted barriers with porosity ranging from 10% to 25% were examined. For the wave conditions and tide level changes tested in this study, the following conclusions can be drawn:

- Increasing the wave height caused the transmission coefficient to decrease and the pneumatic efficiency of energy extraction to increase, but it did not have any noticeable influence on the reflection coefficient.
- Reducing the porosity of the slotted barrier from 25% to 10% increases the drag, viscous dissipation coefficient, and reflection coefficients, and it decreases the transmission coefficient, but it has only a minor influence on the pneumatic efficiency.
- Minimum reflection coefficients occurred when the wave length is about six times the OWC chamber width regardless of the porosity of the slotted barrier.
- For a 10% porosity, a slight increase in the water depth did not produce a significant influence on the parameters studied, and the transmission coefficient varied in a narrow range of 0.5 to 0.75 for the wave periods and water depths tested.

In reality, multiple units of dual-function breakwater are needed to construct a breakwater, and random ocean waves may approach the breakwater at any incident angle. Wave basin tests on a harbor constructed using a row of multiple dual-function breakwaters are planned, where directional irregular waves will be employed. The results will be reported elsewhere.

Author Contributions: Conceptualization, C.C.M.R., M.W. and Z.H.; methodology, C.C.M.R., M.W. and Z.H.; formal analysis, C.C.M.R. and Z.H.; investigation, C.C.M.R., M.W. and Z.H.; resources, Z.H. and P.C.; data curation, C.C.M.R. and Z.H.; writing, C.C.M.R., M.W. and Z.H.; visualization, C.C.M.R., M.W. and Z.H.; supervision, Z.H.; project administration, P.C.; funding acquisition, P.C. All authors have read and agreed to the published version of the manuscript.

Funding: The material presented in this paper is based upon work supported by the Naval Facilities Engineering and Expeditionary Warfare Center (NAVFAC EXWC) under Contract No. N0002419D6400, Task Order No. N0002421F8805. The views, opinions and/or findings expressed are those of the author and should not be interpreted as representing the official views or policies of the US Navy or the U.S. Government.

Data Availability Statement: The data presented in this study are available on request from the corresponding author.

Acknowledgments: The authors thank Shijie Huang, at the University of Hawaii at Manoa, for helping with testing the load cells as well as the wave gauge and pressure sensor data processing. This is SOEST contribution no. 11830.

Conflicts of Interest: The authors declare no conflicts of interest.

References

1. Xu, C.; Huang, Z. A dual-functional wave-power plant for wave-energy extraction and shore protection: A wave-flume study. *Appl. Energy* **2018**, *229*, 963–976. [CrossRef]
2. Takahashi, S. Breakwater Design. In *Handbook of Port and Harbor Engineering: Geotechnical and Structural Aspects*; Springer: Boston, MA, USA, 1997; pp. 951–1043.
3. Carpi, L.; Bicenio, M.; Mucerino, L.; Ferrari, M. Detached breakwaters, yes or not? A modelling approach to evaluate and plan their removal. *Ocean Coast. Manag.* **2021**, *210*, 105668. [CrossRef]
4. Hara, T.; Mei, C.C. Bragg scattering of surface waves by periodic bars: Theory and experiment. *J. Fluid Mech.* **1987**, *178*, 221–241. [CrossRef]
5. Bailard, J.A.; DeVries, J.; Kirby, J.T.; Guza, R.T. Bragg reflection breakwater: A new shore protection method? In *Coastal Engineering 1990*; ASCE: Reston, VA, USA, 1991; pp. 1702–1715.
6. Jeon, C.H.; Cho, Y.S. Bragg reflection of sinusoidal waves due to trapezoidal submerged breakwaters. *Ocean Eng.* **2006**, *33*, 2067–2082. [CrossRef]
7. Li, A.J.; Liu, Y.; Liu, X.; Zhao, Y. Analytical and experimental studies on Bragg scattering of water waves by multiple submerged perforated semi-circular breakwaters. *Ocean Eng.* **2020**, *209*, 107419. [CrossRef]
8. Huang, Z.; Li, Y.; Liu, Y. Hydraulic performance and wave loadings of perforated/slotted coastal structures: A review. *Ocean Eng.* **2011**, *38*, 1031–1053. [CrossRef]
9. Barstow, S.; Mørk, G.; Mollison, D.; Cruz, J. The Wave Energy Resource. In *Ocean Wave Energy: Current Status and Future Prespectives*; Cruz, J., Ed.; Springer: Berlin/Heidelberg, Germany, 2008; pp. 93–132.
10. Falnes, J. A review of wave-energy extraction. *Mar. Struct.* **2007**, *20*, 185–201. [CrossRef]
11. Zhang, Y.; Zhao, Y.; Sun, W.; Li, J. Ocean wave energy converters: Technical principle, device realization, and performance evaluation. *Renew. Sustain. Energy Rev.* **2021**, *141*, 110764. [CrossRef]
12. Falcão, A.F.; Henriques, J.C. Oscillating-water-column wave energy converters and air turbines: A review. *Renew. Energy* **2016**, *85*, 1391–1424. [CrossRef]
13. Xu, C.; Huang, Z. A laboratory study of wave-induced local scour at an emergent pile breakwater. *Ocean Eng.* **2023**, *270*, 113618. [CrossRef]
14. Evans, D.V. The Oscillating Water Column Wave-energy Device. *IMA J. Appl. Math.* **1978**, *22*, 423–433. [CrossRef]
15. Zheng, S.; Antonini, A.; Zhang, Y.; Miles, J.; Greaves, D.; Zhu, G.; Iglesias, G. Hydrodynamic performance of a multi-Oscillating Water Column (OWC) platform. *Appl. Ocean Res.* **2020**, *99*, 102168. [CrossRef]
16. Zhu, S.; Chwang, A.T. Investigations on the reflection behaviour of a slotted seawall. *Coast. Eng.* **2001**, *43*, 93–104. [CrossRef]
17. Huang, Z. Wave interaction with one or two rows of closely spaced rectangular cylinders. *Ocean Eng.* **2007**, *34*, 1584–1591. [CrossRef]
18. Suh, K.D.; Ji, C.H.; Kim, B.H. Closed-form solutions for wave reflection and transmission by vertical slotted barrier. *Coast. Eng.* **2011**, *58*, 1089–1096. [CrossRef]
19. Simonetti, I.; Cappietti, L.; Elsafti, H.; Oumeraci, H. Evaluation of air compressibility effects on the performance of fixed OWC wave energy converters using CFD modelling. *Renew. Energy* **2018**, *119*, 741–753. [CrossRef]
20. Zhang, Y.; Zou, Q.P.; Greaves, D. Air–water two-phase flow modelling of hydrodynamic performance of an oscillating water column device. *Renew. Energy* **2012**, *41*, 159–170. [CrossRef]
21. Wen, H.; Ren, B.; Yu, X. An improved SPH model for turbulent hydrodynamics of a 2D oscillating water chamber. *Ocean Eng.* **2018**, *150*, 152–166. [CrossRef]
22. Didier, E.; Neves, D.R.; Teixeira, P.R.; Dias, J.; Neves, M.G. Smoothed particle hydrodynamics numerical model for modeling an oscillating water chamber. *Ocean Eng.* **2016**, *123*, 397–410. [CrossRef]
23. Setra Systems, Inc. Model 239 | Test and Measurement Pressure Transducer—setra.com. Available online: https://www.setra.com/products/pressure/model-239-high-accuracy-pressure-transducer (accessed on 12 February 2024).

24. Xu, C.; Huang, Z.; Deng, Z. Experimental and theoretical study of a cylindrical oscillating water column device with a quadratic power take-off model. *Appl. Ocean Res.* **2016**, *57*, 19–29. [CrossRef]
25. He, F.; Huang, Z. Characteristics of orifices for modeling nonlinear power take-off in wave-flume tests of oscillating water column devices. *J. Zhejiang Univ. Sci. A* **2017**, *18*, 329–345. [CrossRef]
26. Ulm, N.; Huang, Z.; Cross, P. Experimental Study of a Fixed OWC-Type Wave Energy Converter with a Heave Plate and V-Shaped Channels for Intermediate-Water-Depth Applications. *Energies* **2023**, *16*, 5988. [CrossRef]
27. Goda, Y.; Suzuki, Y. Estimation of incident and reflected waves in random wave experiments. In *Coastal Engineering*; ASCE: Reston, VA, USA, 1976; pp. 828–845.
28. Hunt, J. Viscous damping of waves over an inclined bed in a channel of finite width. *Houille Blanche* **1952**, 836–842. [CrossRef]
29. Dorn, W.G.V. Boundary dissipation of oscillatory waves. *J. Fluid Mech.* **1966**, *24*, 769–779. [CrossRef]
30. Miles, J.W.; Benjamin, T.B. Surface-wave damping in closed basins. *Proc. R. Soc. Lond. Ser. A Math. Phys. Sci.* **1967**, *297*, 459–475. [CrossRef]
31. Ippen, A.T. *Estuary and Coastline Hydrodynamics*; McGraw-Hill Book Company: New York, NY, USA, 1966.
32. Stiassnie, M.; Naheer, E.; Boguslavsky, I. Energy Losses Due to Vortex Shedding from the Lower Edge of a Vertical Plate Attacked by Surface Waves. *Proc. R. Soc. A Math. Phys. Eng. Sci.* **1984**, *396*, 131–142. [CrossRef]
33. Zhao, K.; Wang, Y.; Liu, P.L.F. A guide for selecting periodic water wave theories—Le Méhauté (1976)'s graph revisited. *Coast. Eng.* **2024**, *188*, 104432. [CrossRef]
34. Li, A.-J.; Liu, Y.; Liu, X.; Zhao, Y. Analytical and experimental studies on water wave interaction with a submerged perforated quarter-circular caisson breakwater. *Appl. Ocean Res.* **2020**, *101*, 102267. [CrossRef]
35. He, F.; Huang, Z. Using an Oscillating Water Column Structure to Reduce Wave Reflection from a Vertical Wall. *J. Waterw. Port Coast. Ocean Eng.* **2016**, *142*, 04015021. [CrossRef]
36. Mei, C.C. *The Applied Dynamics of Ocean Surface Waves*; World Scientific: Singapore, 1989; Volume 1.
37. Longuet-Higgins, M.S. On the joint distribution of wave periods and amplitudes in a random wave field. *Proc. R. Soc. Lond. A Math. Phys. Sci.* **1983**, *389*, 241–258.
38. Srokosz, M.; Challenor, P. Joint distributions of wave height and period: A critical comparison. *Ocean Eng.* **1987**, *14*, 295–311. [CrossRef]

Disclaimer/Publisher's Note: The statements, opinions and data contained in all publications are solely those of the individual author(s) and contributor(s) and not of MDPI and/or the editor(s). MDPI and/or the editor(s) disclaim responsibility for any injury to people or property resulting from any ideas, methods, instructions or products referred to in the content.